Article

Cu²⁺−Citrate−Chitosan Complex Nanoparticles for the Chemodynamic Therapy of Lung Cancer

Hechen Sun, Lening Zhang, Nan Zhao, and Hua Xin*

Cite This: *ACS Omega* 2024, 9, 8425−8433

Read Online

ACCESS | 📊 Metrics & More | 📖 Article Recommendations | 🆂🅸 Supporting Information

ABSTRACT: Lung cancer poses a significant threat to human health. Surgical intervention is the preferred treatment modality for lung cancer, but a large number of patients are deprived of the opportunity for surgery for various reasons and are compelled to undergo radiotherapy and chemotherapy, which entail systemic adverse reactions. In recent years, with the advancement of nanomedicine, chemodynamic therapy (CDT) based on free radicals has been extensively investigated. In this study, we fabricated copper−citrate−chitosan composite nanoparticles (CuCC NPs) by encapsulating copper−citrate complexes with natural chitosan polymers, resulting in a substantial reduction in the biotoxicity of copper ions. The CuCC NPs selectively accumulated in tumor tissues through the enhanced permeability and retention effect (EPR) and gradually degraded within the acidic and glutathione (GSH)-rich microenvironment of the tumor, thereby releasing the loaded copper ions. Through CDT, the copper ions converted the overexpressed hydrogen peroxide (H_2O_2) in the tumor tissue into hydroxyl radicals (•OH), leading to the eradication of tumor cells. In animal experiments, CuCC NPs exhibited remarkable efficacy in CDT. Further histopathological and hematological analyses demonstrated that CuCC NPs could induce substantial apoptosis in tumor tissues while maintaining an extremely high level of safety.
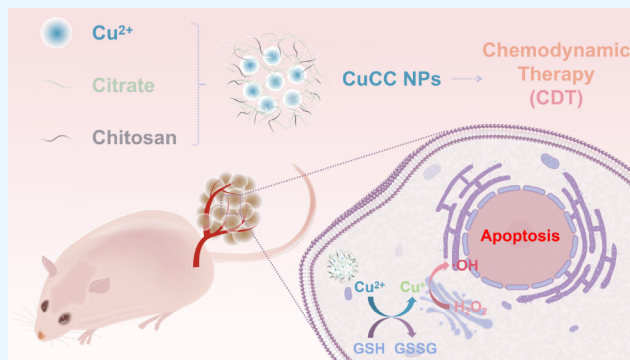
INTRODUCTION

Since the 20th century, cancer has been recognized as one of the major threats to human health. With the increasing aging population, cancer has become the leading public health issue, endangering human life. Lung cancer, in particular, is the malignancy with the highest mortality rate worldwide. According to statistics, in 2020, there were over 2.2 million new cases of lung cancer globally, resulting in over 1.8 million new deaths.[1−3] In the year 2023 alone, it is estimated that there will be over 230,000 new cases of lung cancer in the United States, with a projected death toll of over 120,000.[3] Nonsmall cell lung cancer (NSCLC) represents the predominant histological subtype of lung cancer, accounting for approximately 85% of cases.[4] Surgical intervention is the preferred treatment for early-stage lung cancer; however, a significant number of patients lose the opportunity for surgery due to various reasons.[5] Currently, for this patient population, radiotherapy and chemotherapy are the main treatment modalities.[6,7] However, these systemic therapies have limited tumor specificity and often come with severe systemic adverse reactions. Therefore, there is a pressing need to develop a novel therapeutic approach that can enhance tumor-killing efficacy while simultaneously mitigating systemic adverse reactions. Such an approach would hold significant research value.

In recent years, with the rapid development of nanotechnology, nanomedicine has gained significant attention due to its unique properties. Especially, the emergence of nanomedicine has provided new options for the treatment of tumors.[8−13] Nanomedicine for lung cancer diagnosis and therapy has also been extensively studied,[11,14−19] exhibiting notable advantages such as high safety, specificity, and convenience compared to traditional treatments.[20−29] Chemodynamic therapy (CDT) is an emerging cancer treatment strategy that was first proposed in 2016.[30] In the acidic tumor microenvironment (TME), it utilizes the Fenton reaction or Fenton-like reactions to convert the overexpressed hydrogen peroxide (H_2O_2) into highly cytotoxic hydroxyl radical (•OH) species to kill cancer cells.[31] Since H_2O_2 is predominantly overexpressed in the TME, this effect minimizes damage to normal tissues. Moreover, CDT does not require the introduction of external energy, making it a more convenient approach compared with other therapies. In addition to iron-
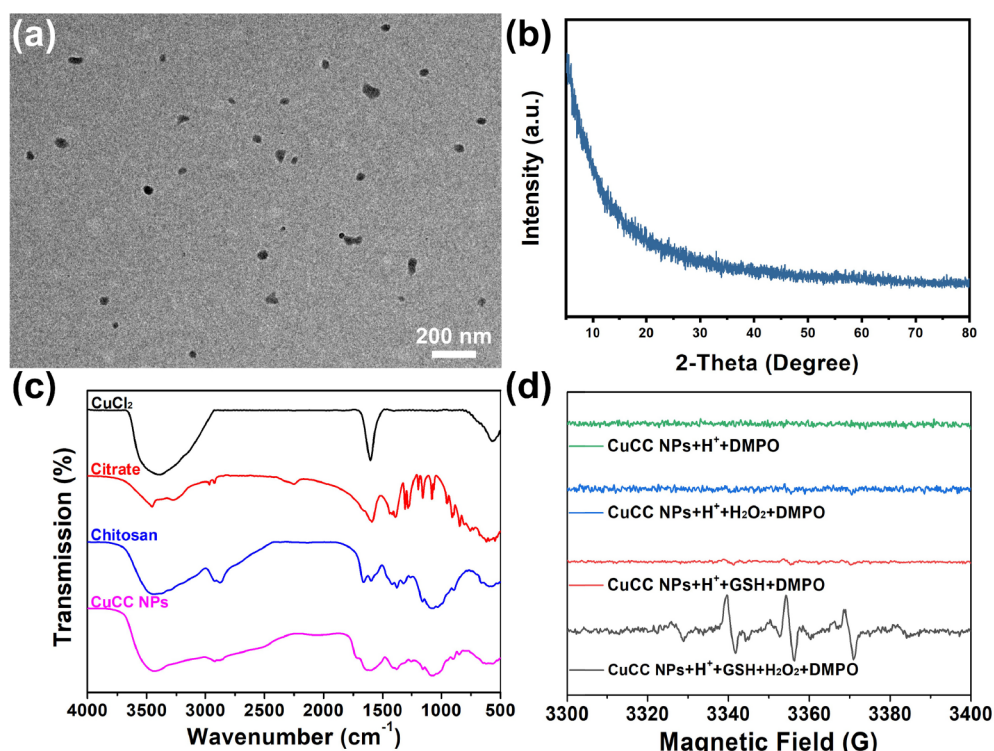
Figure 1. (a) TEM image of CuCC NPs. (b) XRD spectrum of CuCC NPs. (c) FTIR spectrum of CuCC NPs, chitosan, citrate, and CuCl$_2$. (d) ESR spectra of CuCC NPs with different treatments.

based nanomedicines, strategies utilizing copper,[20] manganese,[32] platinum,[22] and other metal elements for CDT through Fenton-like reactions have been proposed. Among these metal elements, copper stands out due to its distinctive characteristics. First, copper is an essential trace element in the body and is required for various physiological processes in almost all cells. It exhibits good tissue compatibility, and appropriate doses of copper do not cause invasive damage to the human body.[33] Second, the optimal pH range for Fenton or Fenton-like reactions is around pH 2−4, while the pH of the tumor microenvironment is around 6. This limits the catalytic efficiency of iron-based CDT particles. However, the redox potential of copper, Cu^{2+}/Cu$^+$ (0.16 V), is significantly lower than that of Fe^{3+}/Fe^{2+}. As a result, the Fenton reaction catalyzed by Cu$^+$ is 160 times more efficient than that of Fe^{2+} ions,[34] significantly enhancing the CDT efficiency of nanomedicines.

However, once the level of free copper exceeds a certain threshold in the body, it can have severe implications for human health, which severely restricts the biological applications of copper-based nanoparticles. Therefore, finding a suitable carrier that can efficiently encapsulate and mitigate the toxicity of copper ions becomes the primary issue to be addressed.[12,35] Chitosan, derived from chitin, is a natural polymer composed of D-glucosamine units and possesses excellent biocompatibility. Chitosan remains stable under neutral conditions but can dissociate into cationic groups in acidic environments. Its surface contains abundant amino and hydroxyl groups, and chitosan can slowly degrade in the human body. Due to these properties, chitosan is often chosen as a drug carrier.[36] However, chitosan exhibits a poor compatibility with Cu^{2+}. Therefore, we selected negatively charged citric acid with three carboxyl groups in the water as a mediator. It can tightly bind to Cu^{2+} through coordination and

can also interact with the cationic groups released by chitosan, thereby facilitating the construction of copper−citrate−chitosan composite nanoparticles (CuCC NPs).

In this context, we synthesized CuCC NPs by using a one-pot method. The use of natural chitosan polymer as a carrier to encapsulate copper−citrate complexes significantly reduced the biotoxicity of free copper. CuCC NPs exhibited an enhanced permeation and retention (EPR) effect, allowing their accumulation in tumor tissues. In response to the acidic and glutathione (GSH)-rich microenvironments of tumor tissues, CuCC NPs underwent slow degradation, releasing the loaded copper ions. These copper ions, through the process of CDT, converted the overexpressed H$_2$O$_2$ in tumor tissues into ●OH, resulting in the eradication of tumor cells. In the simulated TME *in vitro*, copper-loaded CuCC NPs effectively generated ●OH. In cellular and animal experiments, CuCC NPs demonstrated excellent CDT efficacy against lung cancer. Further histopathological and hematological analyses indicated that CuCC NPs induced significant apoptosis in tumor tissues through CDT, while exhibiting favorable biocompatibility and safety.

■ RESULTS AND DISCUSSIONS

In this study, we synthesized Cu^{2+}-loaded CuCC NPs by using the conventional ion gelation method. Prior to adjusting the pH of the mixed solution, the solution exhibited a pale blue color. Upon further adjustment to around pH 3.25, the solution gradually turned bluish-green, and the occurrence of the Tyndall effect upon laser irradiation confirmed the successful synthesis of CuCC NPs. Finally, pure NPs were obtained through a dialysis method (Figure S1). Transmission electron microscopy (TEM) revealed the presence of nearly spherical nanoparticles with an approximate diameter of 42 nm (Figure 1a). Subsequent dynamic light scattering (DLS)

measurements yielded an average particle size of 88 nm (Figure S2), slightly larger than the observations under TEM. X-ray diffraction (XRD) analysis did not exhibit distinct diffraction peaks, suggesting the amorphous nature of the CuCC NPs (Figure 1b). The characteristic absorption peak belonging to Cu^{2+} at 1611 cm^{-1}, the characteristic absorption peak belonging to citrate at 1157 and 2925 cm^{-1}, and the characteristic absorption peak belonging to chitosan at 2868 and 3438 cm^{-1}, all appeared in the Fourier-transform infrared spectroscopy (FTIR) spectrogram of CuCC NPs, proving the existence of Cu^{2+}, citrate, and chitosan in CuCC NPs (Figure 1c).

In a slightly acidic mixture with a pH 6.0, CuCC NPs could effectively clear GSH. In the solution where the initial concentration of GSH is 2 mmol/L, the consumption of GSH increased rapidly along with the increased concentration of CuCC NPs, which was conducive to the increase of Cu^+ concentration and consequent catalytic capacity (Figure S3). Under the catalysis of Cu^+, H_2O_2 can be converted into •OH. Therefore, the generation of •OH by CuCC NPs was validated. 5,5-dimethyl-1-pyrroline-N-oxide (DMPO) was employed as the •OH scavenger, and the generation of •OH was detected by electron spin resonance (ESR). As indicated by the ESR results, the appearance of a 1:2:2:1 peak was observed only in the mixture (pH 6.0) containing CuCC NPs (200 μg/mL), GSH (2 mmol/L), and H_2O_2 (100 μmol/L), indicating the generation of •OH (Figure 1d). This finding suggests that CuCC NPs can respond to the TME and generate •OH through the Fenton-like reaction, which makes them suitable for CDT.

Furthermore, in the additional colloidal stability test, CuCC NPs exhibited excellent performance, maintaining good dispersibility after coincubation with pure water, PBS, and complete culture medium for 3 days (Figure S4). Good colloidal stability was conducive to the development of subsequent biological research.

Encouraged by the excellent CDT performance of CuCC NPs in vitro, further investigations were conducted to evaluate their behavior in cells. First, the safety of CuCC NPs was validated by coincubating human normal bronchial epithelial cells (BEAS-2B) with different concentrations of CuCC NPs (0, 50, 100, 150, and 200 μg/mL) for 24 h, followed by the determination of cell viability using the CCK-8 assay. Even at a drug concentration of 200 μg/mL, the relative cell viability of BEAS-2B cells remained above 77% (Figure 2a). The slight cytotoxicity of the NPs was attributed to the doping of Cu^{2+}. Relevant studies have shown that trace amounts of free Cu^{2+} can kill most cells (Figure S5a), but the mixture of citrate and chitosan almost shows no cytotoxicity (Figure S5b), indicating that the encapsulation of the chitosan polymer confers higher safety to the CuCC NPs. Next, human nonsmall-cell lung cancer cells (A549) were selected as the tumor cell model for therapeutic experiments in vitro. As shown in Figure 2b, with increasing drug concentrations, the relative cell viability gradually decreased, reaching only 28% at a concentration of 200 μg/mL. In order to further investigate the underlying factors contributing to the differential therapeutic outcomes of CuCC NPs on the two cell types, we employed the DCFH-DA probe, which is a fluorescent probe capable of detecting intracellular •OH generation. After entering the cells, DCFH-DA is deacetylated to form nonfluorescent DCFH, which can be oxidized by intracellular •OH to form green fluorescent 2,7-dichlorofluorescein (DCF), with fluorescence levels propor-
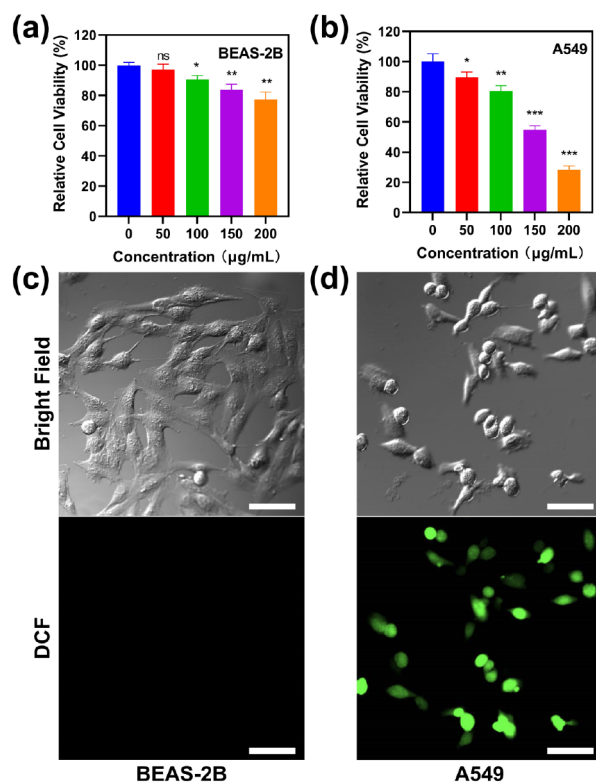
Figure 2. Cytotoxicity of CuCC NPs on (a) BEAS-2B and (b) A549 cells. Coincubation of (c) BEAS-2B and (d) A549 cells with CuCC NPs, followed by CLSM observation of intracellular •OH generation; the scale bar is 50 μm.

tional to the •OH levels. After coincubating A549 and BEAS-2B cells with CuCC NPs for 24 h, the intracellular ROS levels were detected using the DCFH-DA assay kit. As shown in Figure 2c,d, through observation using confocal laser scanning microscopy (CLSM), significant green fluorescence was observed in A549 cells, while no fluorescence was observed in BEAS-2B cells. Consistent with the in vitro experiments, CuCC NPs can selectively respond to the TME within A549 cells, generating •OH to induce tumor cell death while causing minimal damage to normal cells.

And the fluorescence intensity representing ROS levels within A549 cells increased gradually with the increasing coincubation concentration of NPs (Figure 3a). The results
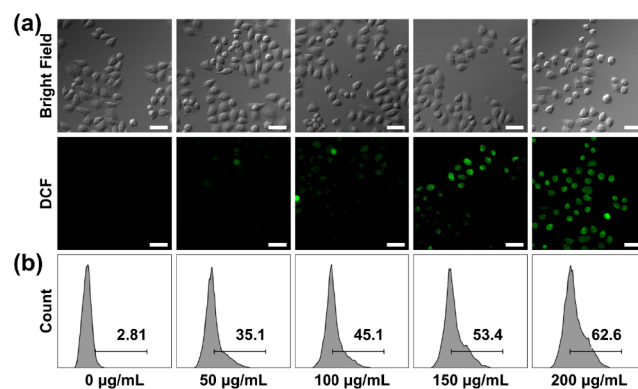
Figure 3. (a) CLSM detection of •OH generation in A549 cells; the scale bar is 50 μm. (b) Flow cytometry analysis of ROS-positive A549 cells after coincubation with CuCC NPs at different concentrations.
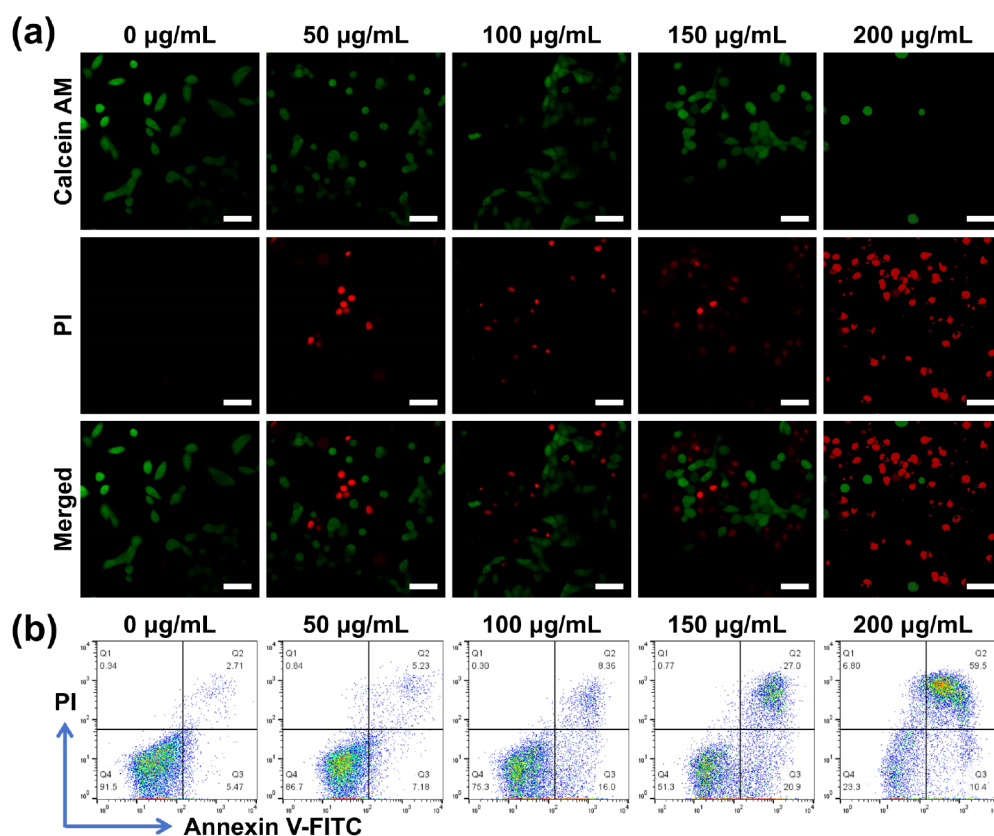
Figure 4. A549 cells were coincubated with CuCC NPs at different concentrations, followed by assessment of cell status using (a) calcein/PI cell viability/cytotoxicity assay kit and (b) annexin-V FITC/PI cell apoptosis assay kit. The scale bar is 50 μm.

from flow cytometry provided a more intuitive demonstration of the trend of ROS intensity with varying NP concentrations. As shown in Figure 3b, as the concentration of CuCC NPs increased, the ratio of ROS-positive cells gradually increased. However, the mixture of citrate and chitosan does not induce ROS production in A549 cells (Figure S6a). Although free Cu^{2+} can promote ROS production, very low concentrations of Cu^{2+} cause changes in the cell morphology (Figure S6b). The high toxicity of Cu^{2+} severely limits its application, which also shows that the way we encapsulate Cu^{2+} in CuCC NPs is correct and necessary. The above results demonstrate that CuCC NPs can selectively generate ROS within A549 cells with concentration-dependent behavior, showcasing excellent CDT efficacy.

Next, we further evaluated the efficacy of CuCC NPs in A549 cells by using a live/dead assay kit. After coincubation of A549 cells with different concentrations of NPs, the cells were stained with Calcein AM and propidium iodide (PI). As shown in Figure 4a, the number of living cells decreased progressively with increasing concentrations of NPs, while the proportion of dead cells increased. The results from the flow cytometry (annexin-V FITC/PI apoptosis assay) also indicated a gradual increase in the proportion of apoptotic cells at the different concentrations of CuCC NPs were 0, 50, 100, 150, and 200 μg/mL, with percentages of 8.5%, 13%, 25%, 50%, and 77%, respectively (Figure 4b). These findings align with the trend observed in A549 cells, where the proportion of ROS-positive cells varied with NP concentration. A series of findings indicate that CuCC NPs exhibit excellent CDT efficacy and safety at the cellular level.

Next, we evaluated the CDT efficacy of CuCC NPs *in vivo*, starting with an assessment of their safety upon administration. Healthy mice of the same age were used as controls, and the indicators of physical function were measured after treatment with CuCC NPs or the citrate−chitosan mixture (Citrate and Chitosan). No significant differences were observed in blood glucose, blood lipids, liver function indicators, kidney function indicators, and serum ion levels between the Citrate and Chitosan, CuCC NPs, and the control groups (Figure S7− S11). These results demonstrate the excellent safety profile of CuCC NPs *in vivo*.

And the accumulation of CuCC NPs at the tumor site was evaluated by determining the content of copper ions using inductively coupled plasma atomic emission spectroscopy (ICP-AES). As shown in Figure S12, after injection of CuCC NPs (100 μL, 2 mg/mL) into A549 tumor-bearing mice, the accumulation rate of CuCC NPs at the tumor site reached 7.19 ± 1.15%ID/g through the EPR effect after 24 h. These results indicate that within 24 h of administration, the NPs efficiently accumulated at the tumor site and can subsequently respond to the TME to generate ●OH for effective CDT.

Finally, we evaluated the therapeutic efficacy of CuCC NPs in A549 animal models over a 15-day treatment period. A549 tumor-bearing mice were divided into three treatment groups: the blank control group, the Citrate and Chitosan group, and the experimental group, which received tail intravenous injections of saline, citrate−chitosan mixed solution, and CuCC NPs. As shown in Figure 5a, the tumor volume in the blank control group rapidly increased, with an average volume exceeding 700 mm^3 after 15 days. The Citrate−Chitosan group exhibited a similar tumor growth trend, indicating that the
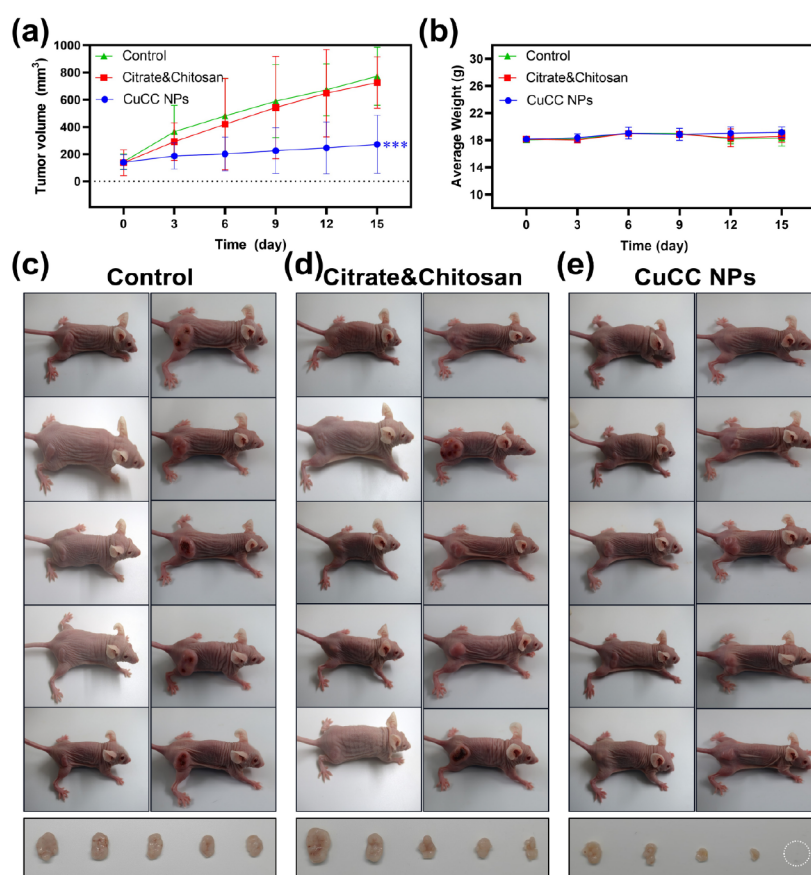
Figure 5. CDT treatment *in vivo*: (a) Tumor volume curves for each group. (b) Average body weight curves for each group. (c−e) A549 tumor-bearing mice before treatment (on the left) and after treatment (on the right) and photographs of tumors in different groups after the treatment (below).

citrate−chitosan mixed solution alone was not effective in inhibiting tumor growth. In contrast, the CuCC NP treatment group showed significant therapeutic efficacy with noticeable tumor growth inhibition observed in all mice, including complete eradication of the tumor in one mouse. After 15 days, the average tumor volume in the CuCC NP treatment group was approximately 270 mm³, which was only 38.6% of the average volume in the control group. These results from the animal experiments demonstrate that the application of CuCC NPs can effectively suppress the growth of A549 tumors through CDT.

Further histopathological studies revealed evident apoptosis in the tumor hematoxylin and eosin (H&E)-stained sections treated with CuCC NPs, while the tumor tissues in the control and citrate−chitosan groups remained largely intact (Figure 6a). TUNEL staining can detect the breakdown of nuclear DNA during apoptosis and accurately reflect the degree of apoptosis. The relevant experimental results were highly consistent with the H&E staining results, and the A549 cells in the NP group were largely apoptotic, and the therapeutic effect was significant (Figure 6b). And immunofluorescence experiments were conducted to examine the expression of the apoptosis-related proteins, Bax and Bcl-2, in the tumor tissues after treatment. Compared to the control and Citrate and Chitosan groups, the CuCC NP treatment group exhibited a significant increase in the expression of the proapoptotic protein Bax (Figure 6c), accompanied by a significant decrease in the expression of the antiapoptotic protein Bcl-2 (Figure 6d). The quantitative analysis of the fluorescence intensity

more directly reflected the change in the above protein expression level (Figure S13). Collectively, these results indicate that CuCC NPs, through the EPR effect, accumulate at the tumor site, respond to the tumor microenvironment, undergo CDT, and induce significant apoptosis in A549 tumor cells, thereby inhibiting tumor growth.

Additionally, the body weight of mice in each treatment group was monitored from the first treatment until the end of the study, as shown in Figure 5b. For the first 9 days, the body weight of mice in all three groups steadily increased. However, the subsequent changes in body weight differed among the groups. In the control group and the Citrate and Chitosan group, the rapid proliferation of tumors suppressed the growth of mice, resulting in a gradual decrease in body weight after 9 days. In contrast, mice in the NP treatment group exhibited a consistent trend of weight gain, indicating that NPs effectively inhibited tumor growth while maintaining the overall health. After the completion of treatment, further histopathological examination confirmed the safety of CuCC NPs. Compared to the control group, H&E sections of vital organs (heart, liver, spleen, lung, and kidney) revealed no apparent pathological changes such as tissue apoptosis, necrosis, edema, or inflammatory cell infiltration (Figure S14). These results collectively demonstrate that CuCC NPs can efficiently treat A549 tumors *in vivo* through CDT while exhibiting a high level of safety.
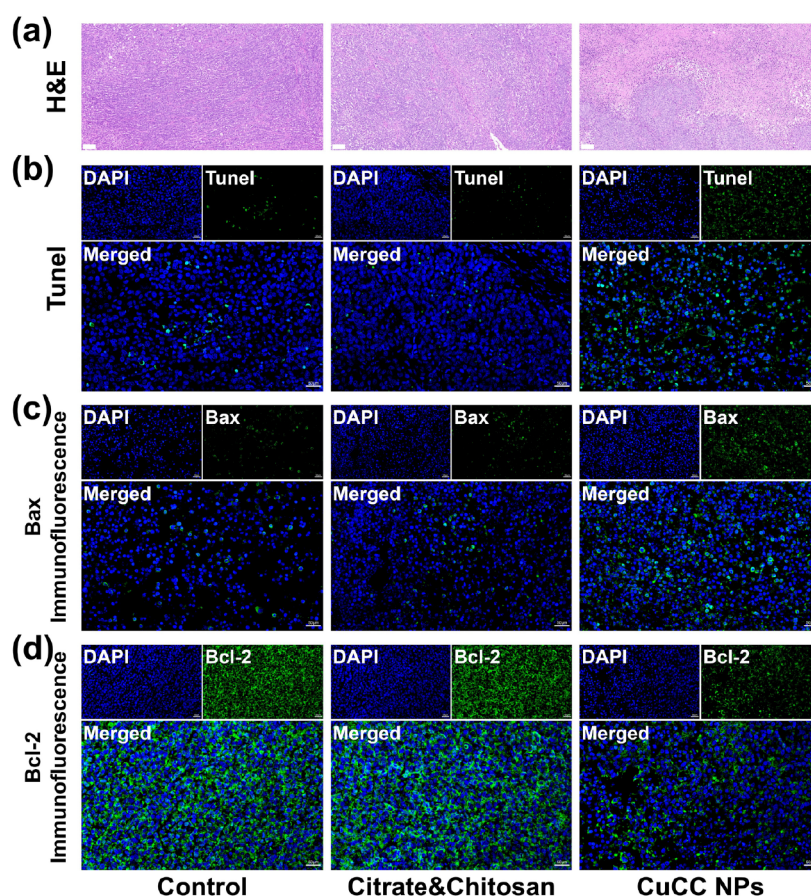
Figure 6. (a) Histological sections of tumor tissues from each group stained with H and E. The scale bar is 100 μm. (b) Tunel-stained sections of tumor tissues from each group. The scale bar of is 50 μm. Immunofluorescence detection of apoptosis-related proteins (c) Bax and (d) Bcl-2 expression. The scale bar of is 50 μm.

CONCLUSIONS

In conclusion, we fabricated CuCC NPs with CDT function. The encapsulation of the chitosan polymer conferred higher tissue compatibility and stability to the nanoparticles. CuCC NPs accumulated in A549 tumor tissue through the EPR effect, with an accumulation rate of 7.19 ± 1.15%ID/g at the tumor site after 24 h of administration. The NPs in the tumor tissue responded to the acidic and GSHe-rich TME, releasing copper ions, which mediated efficient CDT and effectively killed the A549 cells. In animal and cell experiments, CuCC NPs demonstrated an excellent CDT efficacy. Further histopathological, immunofluorescence, and hematological analyses revealed significant apoptosis induced by CDT in the tumor tissue, while no significant damage was observed in normal tissues and organs. CuCC NPs represent a highly efficient and cost-effective CDT-based nanoplatform for the treatment of lung cancer with promising future applications.

EXPERIMENTAL SECTION

Materials. Chitosan with a low molecular weight was purchased from Macklin, and citric acid monohydrate was obtained from Sinopharm Chemical Reagent Co., Ltd. Analytical-grade sodium hydroxide (NaOH), copper chloride dihydrate (CuCl$_2$·2H$_2$O), and DMPO were purchased from Aladdin. The cell culture medium (DMEM) was obtained from Gibco, and fetal bovine serum (FBS) was purchased from Procell. Trypsin digestion solution and an annexin V-FITC/PI

apoptosis detection kit were obtained from Solarbio. The Cell Counting Kit-8 (CCK-8), reactive oxygen species assay kit, and calcein/PI cell viability/cytotoxicity assay kit were all purchased from Beyotime. All reagents were used without further purification after purchase, and all experimental water was deionized water.

Preparation of CuCC NPs. To begin, separate solutions were prepared by dissolving 50 mg of chitosan, 240 mg of CuCl$_2$·2H$_2$O, and 560 mg of citric acid in 100 mL of water. Subsequently, the pH value of the mixed solution was adjusted to approximately 3.25 by using NaOH, facilitating the formation of nanoparticles. Finally, pure CuCC NPs were obtained by dialysis, which effectively removed both the free copper ions and the copper−citrate complexes.

Preparation of Citrate and Chitosan. The synthesis of citrate and chitosan involved the combination of 50 mg of chitosan and 560 mg of citric acid in 100 mL of water. The components were thoroughly mixed to obtain a homogeneous solution.

GSH Depletion *in vitro*. We employed a GSH assay kit to measure the concentration of GSH in the mixed solution. A GSH solution was prepared at a concentration of 2 mmol/L at pH 6.0. After coincubation with varying concentrations (0, 50, 100, 150, 200 μg/L) of CuCC NPs for 24 h, the relative content of GSH in the solution was determined.

ROS Production *in vitro*. DMPO was selected as a free radical scavenger to detect the generation of ROS using ESR. The experiment was divided into four groups: (1) CuCC NPs

(200 μg/mL) + H$^+$ (pH = 6.0) + DMPO (10 μL/mL); (2) CuCC NPs (200 μg/mL) + H$^+$ (pH = 6.0) + H$_2$O$_2$ (100 μmol/L) + DMPO (10 μL/mL); (3) CuCC NPs (200 μg/mL) + H$^+$ (pH = 6.0) + GSH (2 mmol/L) + DMPO (10 μL/mL); and (4) CuCC NPs (200 μg/mL) + H$^+$ (pH = 6.0) + GSH (2 mmol/L) + H$_2$O$_2$ (100 μmol/L) + DMPO (10 μL/mL).

Cell Experiments *In Vitro*. *Cell Culture.* Both BEAS-2B and A549 cells were cultured in DMEM complete medium containing 10% FBS and 1% antibiotics (penicillin and streptomycin) at 37 °C in a humidified incubator with 5% CO$_2$ and 95% air.

Cell Viability Assessment. BEAS-2B and A549 cells were separately coincubated with different concentrations of CuCC NPs (0, 50, 100, and 200 μg/mL dissolved in complete medium) for 24 h. Cell relative viability was determined by measuring the absorbance at 450 nm by using a CCK-8 assay kit.

Intracellular ROS Generation. BEAS-2B and A549 cells were coincubated with different concentrations of CuCC NPs for 24 h. After the culture medium was removed, DCFH-DA (10 μmol, dissolved in serum-free DMEM) was added and further incubated for 30 min. The fluorescence intensity of DCFH was observed by using CLSM or analyzed by flow cytometry after digestion to detect the proportion of DCFH-positive cells.

Cell Viability and Death Assessment. A549 cells were cocultured with different concentrations of CuCC NPs for 24 h, followed by double staining with the cell viability/death assay kit using Calcein AM and PI. The cells were then observed under CLSM.

Cell Apoptosis Detection. A549 cells were cocultured with different concentrations of CuCC NPs for 24 h, followed by double staining with annexin-V FITC and PI. Flow cytometry was used to analyze cell apoptosis.

Safety *in vivo*. Nine mice (age-matched healthy mice) were divided into the experimental group, Citrate and Chitosan group, and control group. They were injected via the tail vein with 100 μL of CuCC NP solution (2 mg/mL), Citrate and Chitosan solution (Citric acid, 1.84 mg/mL and Chitosan, 0.16 mg/mL), and normal saline solution, respectively. The dosage was calculated as 10 mg per kilogram of body weight. After 24 h of administration, the blood glucose, blood lipid, liver function, kidney function, and ion indicators of each mouse were measured.

Accumulation Rate of CuCC NPs. Three A549 tumor-bearing mice were injected with 100 μL of CuCC NP solution with a concentration of 2 mg/mL via the tail vein. After 24 h, the mice were euthanized and dissected. The tumors were weighed and dissolved in aqua regia for copper ion analysis using ICP-AES.

Animal Experiments. All animal experiments related to this study were conducted in accordance with the Guidelines for the Care and Use of Laboratory Animals of Jilin University and approved by the Animal Ethics Committee of the First Hospital of Jilin University. Fifteen BALB/c nude mice (6 weeks old, female) were purchased from Beijing Vital River Laboratory Animal Technology Co., Ltd. To establish the NSCLC model, after the mice acclimated to the environment, 1.0×10^6 A549 cells in 150 μL cell suspension were subcutaneously injected into the right buttock of each mouse. When the average tumor volume reached 140 mm^3, the A549 tumor-bearing mice were divided into three groups:

(1) control, (2) Citrate and Chitosan, and (3) experimental. They were, respectively, injected with 100 μL physiological saline solution, Citrate and Chitosan solution (Citric acid 1.84 mg/mL, Chitosan 0.16 mg/mL), and CuCC NPs solution (2 mg/mL) via the tail vein. Over the next 15 days, the mice were administered the treatments every 3 days, and their body weight and tumor volume ($V = 1/2LS^2$ mm^3, L represents the length of long axis and S represents the length of short axis) were measured. After 15 days, photographs were taken of each group of mice, followed by euthanasia and dissection. The tumors from each group were photographed, and H&E, TUNEL staining, and immunofluorescence experiments of Bax and Bcl-2 were performed. The major organs (heart, liver, spleen, lung, and kidney) were preserved in tissue fixative and subjected to Hand E staining.

Characterization. We captured TEM images using a Hitachi HT7800. The FTIR spectra of the materials were acquired by using a Bruker VERTEX 80 V infrared spectrometer. The hydrated particle size was measured using a Malvern Zetasizer NanoZS. Flow cytometry analysis was performed using the CytoFLEX system from Beckman Coulter. We selected a PerkinElmer Optima 3300DV instrument for ICP-AES analysis. Fluorescence images were obtained using the Olympus FV1000 confocal laser scanning microscope. ESR spectra were obtained by using a Bruker ELEXSYS spectrometer. XRD data were obtained by using a PANalytical BV X-ray diffractometer.

■ ASSOCIATED CONTENT

Ⓢ Supporting Information

The Supporting Information is available free of charge at https://pubs.acs.org/doi/10.1021/acsomega.3c09619.

Additional photos of mixed solution, DLS, cytotoxicity, colloidal stability, CLSM images, blood lipid, liver function, renal function, serum ion, accumulation rate, quantitative analysis of immunofluorescence, and H and E stained primary organ slices of mice (PDF)

■ AUTHOR INFORMATION

Corresponding Author

Hua Xin — *Department of Thoracic Surgery, China-Japan Union Hospital of Jilin University, Changchun 130031, PR China*; Email: xhua@jlu.edu.cn

Authors

Hechen Sun — *Department of Thoracic Surgery, China-Japan Union Hospital of Jilin University, Changchun 130031, PR China*; ⓞ orcid.org/0009-0008-0408-2986

Lening Zhang — *Department of Thoracic Surgery, China-Japan Union Hospital of Jilin University, Changchun 130031, PR China*

Nan Zhao — *Department of Thoracic Surgery, China-Japan Union Hospital of Jilin University, Changchun 130031, PR China*

Complete contact information is available at:
https://pubs.acs.org/10.1021/acsomega.3c09619

Author Contributions

H.X. proposed and supervised the project. H.X. and H.S. designed and performed the experiments. H.S. wrote the paper. L.Z. and N.Z. participated in most experiments. All authors have given approval to the final version of the manuscript.

Notes

The authors declare no competing financial interest.

REFERENCES

(1) Xia, C.; Dong, X.; Li, H.; Cao, M.; Sun, D.; He, S.; Yang, F.; Yan, X.; Zhang, S.; Li, N.; et al. Cancer statistics in China and United States, 2022: profiles, trends, and determinants. *Chin. Med. J. (Engl)* **2022**, *135*, 584−590.

(2) Sung, H.; Ferlay, J.; Siegel, R. L.; Laversanne, M.; Soerjomataram, I.; Jemal, A.; Bray, F. Global cancer statistics 2020: GLOBOCAN estimates of incidence and mortality worldwide for 36 cancers in 185 countries. *Ca-Cancer J. Clin.* **2021**, *71*, 209−249.

(3) Siegel, R. L.; Miller, K. D.; Wagle, N. S.; Jemal, A. Cancer statistics, 2023. *Ca-Cancer J. Clin.* **2023**, *73*, 17−48.

(4) Duma, N.; Santana-Davila, R.; Molina, J. R. Non−Small Cell Lung Cancer: Epidemiology, Screening, Diagnosis, and Treatment. *Mayo Clin. Proc.* **2019**, *94*, 1623−1640.

(5) El-Sherif, A.; Gooding, W. E.; Santos, R.; Pettiford, B.; Ferson, P. F.; Fernando, H. C.; Urda, S. J.; Luketich, J. D.; Landreneau, R. J. Outcomes of sublobar resection versus lobectomy for stage I non-small cell lung cancer: A 13-year analysis. *Annals of Thoracic Surgery* **2006**, *82*, 408−416.

(6) Higgins, K. A.; Puri, S.; Gray, J. E. Systemic and Radiation Therapy Approaches for Locally Advanced Non-Small-Cell Lung Cancer. *J. Clin Oncol.* **2022**, *40*, 576−585.

(7) Park, K.; Vansteenkiste, J.; Lee, K. H.; Pentheroudakis, G.; Zhou, C.; Prabhash, K.; Seto, T.; Voon, P. J.; Tan, D. S. W.; Yang, J. C. H.; et al. Pan-Asian adapted ESMO Clinical Practice Guidelines for the management of patients with locally-advanced unresectable non-small-cell lung cancer: A KSMO-ESMO initiative endorsed by CSCO, ISMPO, JSMO, MOS, SSO and TOS. *Ann. Oncol.* **2020**, *31*, 191−201.

(8) Li, X.; Chen, L.; Luan, S.; Zhou, J.; Xiao, X.; Yang, Y.; Mao, C.; Fang, P.; Chen, L.; Zeng, X.; et al. The development and progress of nanomedicine for esophageal cancer diagnosis and treatment. *Semin. Cancer Biol.* **2022**, *86*, 873−885.

(9) Fang, R. H.; Gao, W.; Zhang, L. Targeting drugs to tumours using cell membrane-coated nanoparticles. *Nat. Rev. Clin. Oncol.* **2023**, *20*, 33−48.

(10) Fan, D.; Cao, Y.; Cao, M.; Wang, Y.; Cao, Y.; Gong, T. Nanomedicine in cancer therapy. *Signal Transduction Targeted Ther.* **2023**, *8*, 293.

(11) Shi, M.; Gu, A.; Tu, H.; Huang, C.; Wang, H.; Yu, Z.; Wang, X.; Cao, L.; Shu, Y.; Yang, R.; et al. Comparing nanoparticle polymeric micellar paclitaxel and solvent-based paclitaxel as first-line treatment of advanced non-small-cell lung cancer: an open-label, randomized, multicenter, phase III trial. *Ann. Oncol.* **2021**, *32*, 85−96.

(12) Yang, J.; Ding, J. Nanoantidotes: A Detoxification System More Applicable to Clinical Practice. *BME Front.* **2023**, *2023*, 0020.

(13) Liu, S.; Zhang, M.; Jin, H.; Wang, Z.; Liu, Y.; Zhang, S.; Zhang, H. Iron-Containing Protein-Mimic Supramolecular Iron Delivery Systems for Ferroptosis Tumor Therapy. *J. Am. Chem. Soc.* **2023**, *145*, 160−170.

(14) Yoneshima, Y.; Morita, S.; Ando, M.; Nakamura, A.; Iwasawa, S.; Yoshioka, H.; Goto, Y.; Takeshita, M.; Harada, T.; Hirano, K.; et al. Phase 3 Trial Comparing Nanoparticle Albumin-Bound Paclitaxel With Docetaxel for Previously Treated Advanced NSCLC. *J. Thorac. Oncol.* **2021**, *16*, 1523−1532.

(15) Spigel, D. R.; Jotte, R. M.; Aix, S. P.; Gressot, L.; Morgensztern, D.; McCleod, M.; Socinski, M. A.; Daniel, D.; Juan-Vidal, O.; Mileham, K. F.; et al. Nanoparticle Albumin-bound Paclitaxel Plus Carboplatin Induction Followed by Nanoparticle Albumin-bound Paclitaxel Maintenance in Squamous Non-Small-cell Lung Cancer (ABOUND.sqm): A Phase III Randomized Clinical Trial. *Clin. Lung Cancer* **2021**, *22*, 6−15.

(16) Morgensztern, D.; Cobo, M.; Aix, S. P.; Postmus, P. E.; Lewanski, C. R.; Bennouna, J.; Fischer, J. R.; Juan-Vidal, O.; Stewart, D. J.; Fasola, G.; et al. ABOUND.2L+: A randomized phase 2 study of nanoparticle albumin-bound paclitaxel with or without CC-486 as second-line treatment for advanced nonsquamous non-small cell lung cancer (NSCLC). *Cancer* **2018**, *124*, 4667−4675.

(17) Lu, J.; Gu, A.; Wang, W.; Huang, A.; Han, B.; Zhong, H. Polymeric micellar paclitaxel (Pm-Pac) prolonged overall survival for NSCLC patients without pleural metastasis. *Int. J. Pharm.* **2022**, *623*, 121961.

(18) Boyacioglu, O.; Bilgic, E.; Varan, C.; Bilensoy, E.; Nemutlu, E.; Sevim, D.; Kocaefe, C.; Korkusuz, P. ACPA decreases non-small cell lung cancer line growth through Akt/PI3K and JNK pathways in vitro. *Cell Death Dis.* **2021**, *12*, 56.

(19) Akiyama, N.; Karayama, M.; Inui, N.; Yasui, H.; Hozumi, H.; Suzuki, Y.; Furuhashi, K.; Fujisawa, T.; Enomoto, N.; Nakamura, Y.; et al. Switch maintenance therapy with S-1 after induction therapy with carboplatin and nanoparticle albumin-bound paclitaxel in advanced lung squamous cell carcinoma. *Invest. New Drugs* **2019**, *37*, 531−537.

(20) An, L.; Wang, C.; Tian, Q.; Tao, C.; Xue, F.; Yang, S.; Zhou, X.; Chen, X.; Huang, G. NIR-II laser-mediated photo-Fenton-like reaction via plasmonic Cu9S8 for immunotherapy enhancement. *Nano Today* **2022**, *43*, 101397.

(21) Chen, Q.; Zhou, J.; Chen, Z.; Luo, Q.; Xu, J.; Song, G. Tumor-Specific Expansion of Oxidative Stress by Glutathione Depletion and Use of a Fenton Nanoagent for Enhanced Chemodynamic Therapy. *ACS Appl. Mater. Interfaces* **2019**, *11*, 30551−30565.

(22) Chen, Y.; Yao, Y.; Zhou, X.; Liao, C.; Dai, X.; Liu, J.; Yu, Y.; Zhang, S. Cascade-Reaction-Based Nanodrug for Combined Chemo/Starvation/Chemodynamic Therapy against Multidrug-Resistant Tumors. *ACS Appl. Mater. Interfaces* **2019**, *11*, 46112−46123.

(23) Cui, M.; Zhang, H.-R.; Ouyang, F.; Guo, Y.-Q.; Li, R.-F.; Duan, S.-F.; Xiong, T.-D.; Wang, Y.-L.; Wang, X.-Q. Dual Enzyme-Like Performances of PLGA Grafted Maghemite Nanocrystals and Their Synergistic Chemo/Chemodynamic Treatment for Human Lung Adenocarcinoma A549 Cells. *J. Biomed. Nanotechnol.* **2021**, *17*, 1007−1019.

(24) Hu, Z.-E.; Li, J.; Wu, Z.-N.; Wei, Y.-J.; Liu, Y.-H.; Wang, N.; Yu, X.-Q. One-Pot Synthesis-Biocompatible Copper-Tripeptide Complex as a Nanocatalytic Medicine to Enhance Chemodynamic Therapy. *ACS Biomater. Sci. Eng.* **2021**, *7*, 1394−1402.

(25) Chen, J.; Wang, X.; Zhang, Y.; Zhang, S.; Liu, H.; Zhang, J.; Feng, H.; Li, B.; Wu, X.; Gao, Y.; et al. A redox-triggered C-centered free radicals nanogenerator for self-enhanced magnetic resonance imaging and chemodynamic therapy. *Biomaterials* **2021**, *266*, 120457.

(26) Cai, P.; Yang, W.; He, Z.; Jia, H.; Wang, H.; Zhao, W.; Gao, L.; Zhang, Z.; Gao, F.; Gao, X. A chlorin-lipid nanovesicle nucleus drug for amplified therapeutic effects of lung cancer by internal radiotherapy combined with the Cerenkov radiation-induced photodynamic therapy. *Biomater. Sci.* **2020**, *8*, 4841−4851.

(27) Cai, X.; Luo, Y.; Song, Y.; Liu, D.; Yan, H.; Li, H.; Du, D.; Zhu, C.; Lin, Y. Integrating in situ formation of nanozymes with three-dimensional dendritic mesoporous silica nanospheres for hypoxia-overcoming photodynamic therapy. *Nanoscale* **2018**, *10*, 22937−22945.

(28) Chang, J.-E.; Cho, H.-J.; Jheon, S. Anticancer Efficacy of Photodynamic Therapy with Lung Cancer-Targeted Nanoparticles. *J. Visualized Exp.* **2016**, *118*, 54865.

(29) Chang, Y.; Li, X.; Zhang, L.; Xia, L.; Liu, X.; Li, C.; Zhang, Y.; Tu, L.; Xue, B.; Zhao, H.; et al. Precise Photodynamic Therapy of Cancer via Subcellular Dynamic Tracing of Dual-loaded Upconversion Nanophotosensitizers. *Sci. Rep.* **2017**, *7*, 45633.

(30) Zhang, C.; Bu, W.; Ni, D.; Zhang, S.; Li, Q.; Yao, Z.; Zhang, J.; Yao, H.; Wang, Z.; Shi, J. Synthesis of Iron Nanometallic Glasses and Their Application in Cancer Therapy by a Localized Fenton Reaction. *Angew. Chem., Int. Ed. Engl.* **2016**, *55*, 2101−2106.

(31) Yang, N.; Cao, C.; Lv, X.; Zhang, T.; Shao, J.; Song, X.; Wang, W.; Chen, P.; Huang, W.; Dong, X. Photo-facilitated chemodynamic therapeutic agents: Synthesis, mechanisms, and biomedical applications. *BMEMat* **2023**, *1*, No. e12005.

(32) Lin, L.; Yu, J.; Lu, H.; Wei, Z.; Chao, Z.; Wang, Z.; Wu, W.; Jiang, H.; Tian, L. Mn-DNA coordination of nanoparticles for efficient chemodynamic therapy. *Chem. Commun.* **2021**, *57*, 1734−1737.

(33) Chen, L.; Min, J.; Wang, F. Copper homeostasis and cuproptosis in health and disease. *Signal Transduction Targeted Ther.* **2022**, *7*, 378.

(34) Brillas, E.; Baños, M. A.; Camps, S.; Arias, C.; Cabot, P. L.; Garrido, J. A.; Rodríguez, R. M. Catalytic effect of Fe^{2+}, Cu^{2+} and UVA light on the electrochemical degradation of nitrobenzene using an oxygen-diffusion cathode. *New J. Chem.* **2004**, *28*, 314−322.

(35) Yang, G.; Liu, Y.; Chen, J.; Ding, J.; Chen, X. Self-Adaptive Nanomaterials for Rational Drug Delivery in Cancer Therapy. *Acc. Mater. Res.* **2022**, *3*, 1232−1247.

(36) Yang, J.; Li, H.; Zou, H.; Ding, J. Polymer Nanoantidotes. *Chem. - Eur. J.* **2023**, *29*, No. e202301107.